Uncertainty quantification in littoral erosion

Bijan Mohammadi

UNCERTAINTY QUANTIFICATION IN LITTORAL EROSION

BIJAN MOHAMMADI

UNIVERSITÉ DE MONTPELLIER, MATHÉMATIQUES (IMAG)

CC51, 34095 MONTPELLIER, FRANCE

TEL: +33467143562 - FAX:+33467143558
BIJAN.MOHAMMADI@UMONTPELLIER.FR

Abstract. We aim at quantifying the impact of flow state uncertainties in littoral erosion to provide confidence bounds on deterministic predictions of bottom morphodynamics. Two constructions of the bathymetry standard deviation are discussed. The first construction involves directional quantile-based extreme scenarios using what is known on the flow state Probability Density Function (PDF) from on site observations. We compare this construction to a second cumulative one using the gradient by adjoint of a functional involving the energy of the system. These ingredients are illustrated for two models for the interaction between a soft bed and a flow in a shallow domain. Our aim is to keep the computational complexity comparable to the deterministic simulations taking advantage of what already available in our simulation toolbox.

1. Introduction

Littoral transformations represent obviously major societal concerns as more than two third of sand beaches worldwide face erosion or accretion with growing trends due to expected rises in the sea levels. Tremendous efforts are dedicated to the understanding of these mechanisms to help their prediction and possibly to develop protection or attenuation devices.

The literature on coastal morphodynamics is huge [12, 11, 37, 13, 49] and concerns, for instance, dunes morphodynamics, sediment transports using fluid-induced shear in the sediment modelling, sea bed friction and the feedback of bed shapes on the

Key words and phrases. Backward propagation, quantile, uncertainty, littoral morphodynamics, Shallow water equations, sensitivity analysis, worst-case analysis.

flow, global beach morphodynamics based on long and cross-shore fluxes and beach lines morphodynamics. Hence, coastal morphodynamics occur over a broad range of time and length scales. Some events take place over small space and time scales such as the removal of sediment from the toe of coastal structures which often occurs and recovers completely during the course of a single tide (hourly basis). The next time and space scales concern storm response lasting for a few tides (say daily basis). Here the beach can be modified both long and cross-shore by hundreds of meters. Recovery between storms will take longer (weekly basis). This classification can continue with seasonal and inter-annual variability etc. In general, the spatial scale increases with the time scale and therefore long-shore transport gains in importance over cross-shore with increasing time scale. The physical models we use in this work are valid for time scales of a few days and do not account for seasonal and inter-annual variabilities. However, the proposed Uncertainty Quantification (UQ) procedures remain valid and can be used with more general models.

In the past, we used minimization principle to design defense structures against beach erosion [27, 28, 14]. In these works, the designed structures were independent of time and built once for all. We also considered situations where the structure changes in time. In particular, we considered the sea bed as a structure with low stiffness with the fundamental assumption that outside storm periods the bed adapts to the flow by some sort of minimal sand transport in order to minimize the wave energy [3, 4]. This formulation permits the application of concepts from control theory to the evolution of sand beds. We also showed how to define extreme scenarios using the theory of quantiles when the bed porosity is seen as a random variable with known probability density function [45].

In this work we would like to extend our uncertainty analysis to account for flow state uncertainties which can be by nature either aleatoric and/or epistemic. The former comes, for instance, from non reducible variability in the definition of incoming waves, and the latter from imperfect models or numerical procedures [41, 43].

In particular, we would like to address one aspect of UQ for a parameter ψ when a target state u^* used in an inverse problem is uncertain. This is the case, for instance, minimizing $j(\psi) = \|u(\psi) - u^*\|$ to reduce the distance(in some suitable norm) between a model state $u(\psi)$ and uncertain observations u^*. This work therefore concerns backward uncertainty propagation[1] and not forward as the aim is to propagate backward the uncertainty on the state (known or assumed) into the optimization parameters (here the shape of the bottom). This is similar to a shape optimization problem for an unsteady flow by a gradient method and we are interested by the uncertainty on the optimal shape knowing the uncertainty on the computed or observed state (here the water height). Monte Carlo approaches, or accelerated versions of them like the multi-level Monte Carlo method [21], are usually for forward propagation. Typically a multi-level Monte Carlo method has been used in [38] for the forward propagation of bathymetry uncertainties into the shallow water solution. One could consider reverse Monte Carlo method which are similar to Metropolis algorithms for inverse problems, or backward Monte Carlo methods such as the Markov Chain Monte Carlo (MCMC)[35] or, of course, Ensemble Kalman Filters (EnKF) [16, 43]. These permit to propagate backward the uncertainty on the observation into the parameters but their cost is high especially with these large dimensional problems where the uncertainty is on the state and distributed all over the domain.

Our goal is to propose low-complexity evaluations of Cov_ψ the covariance matrix of ψ knowing Cov_{u^*}. A first approach uses quantiles and builds directional extreme scenarios for the state from which an approximation of the shape covariance matrix is obtained after two extra inversions. This is similar to the approach adopted in [45]

[1] Forward uncertainty propagation aims at defining a probability density function for a functional $j(\psi)$ knowing those of optimization parameters ψ. This can be done, for instance, through Monte Carlo simulations or a separation between deterministic and stochastic features using the Karhunen-Loeve theory (polynomial chaos theory belongs to this class)[19, 58, 20, 56]. Backward propagation aims at reducing models bias or calibrating models parameters knowing the probability density function of j [1, 6, 33, 54, 31, 7]. This can be seen as a minimization problem and Kalman filters [32] give, for instance, an elegant framework for this inversion assimilating the uncertainties on the observations.

but applied not to the sand porosity but to the state or observations. This approximation is compared to a cumulative construction of the variance during optimization iterations assuming a local linear relationship between the control parameter (here the bottom) and the state.

In terms of calculation complexity and code development, we would like to achieve this without any sampling of a large dimension space. Also, we would like the approaches to be feasible at a cost nearly comparable to a single deterministic minimization. Finally, we would like both approaches to only use what already available in terms of code and not to require intense new developments. This makes them comparable to Monte Carlo type constructions in term of coding complexity but for reverse propagation.

The paper starts recalling the general minimization framework in which our fluid-structure coupling is cast. We describe how state variability can be accounted for in this formulation. Then the two derivations of the bottom covariance matrix are introduced. These ingredients are then illustrated on a model problem and for a more realistic coupling involving the shallow water equations.

2. General settings

We are interested in a class of minimization problems where the cost function involves a parameter u^* not being an optimization parameter:

$$\min_{\psi \in \mathbf{O}_{ad}} j(\psi, u^*), \;\; u^* \in \mathbf{I} \subset \mathbb{R}^p, \mathbf{O}_{ad} \subset \mathbb{R}^n. \tag{1}$$

where ψ is the optimization parameter (here the bed parameterization) belonging to $\mathbf{O}_{ad}$ the optimization admissible domain [46]. This is a very general context and we visited it to address robustness issues in optimization with respect to ψ and u^* [42, 40, 41, 39]. In this work we are interested in functionals j of the form:

$$j(\psi, u^*) = f(\psi, u(\psi)) + \frac{1}{2}\|\Pi u(\psi) - u^*\|^2, \tag{2}$$

where the flow state $u(\psi) \in \mathbb{R}^N$ is solution of a state equation $F(u(\psi)) = 0$ (here a flow model) and operator $\Pi : \mathbb{R}^N \to R^p$ makes the state available at data locations (e.g. an interpolation operator).

2.1. **Uncertain data.** We assume that the data u^* are uncertain, independent and given by their probability density functions here assumed Gaussian $\mathcal{N}(\mu_i, \sigma_i^2),\ i = 1, ..., p$ with mean μ_i and variance of σ_i^2. The covariance matrix Cov_{u^*} is therefore diagonal. Our aim is to use the information on the uncertainty on the observation data u^* to estimate the uncertainty on ψ.

The simplest way to measure the effect of these uncertainties on the inversion result is to proceed with some Monte Carlo like simulations (which we will call inverse Monte Carlo in section 6). This means we proceed with M independent inversions for M data sets defined by independent choices compatible with the PDF of u^* given by:

$$\mathcal{N}(\mu_i, \sigma_i^2) \to (u_i^*)^m, \quad i = 1, ..., p, \quad m = 1, ..., M.$$

These independent simulations will produce M optimal control parameters $\psi_{opt}^m,\ m = 1, ..., M$ from which statistical moments can be defined (typically the mean and variance) with a rate of convergence in $M^{-1/2}$ independent of the size p. Of course, such generation of scenarios is very computationally demanding even if the calculations are independent and manageable in parallel. As discussed in the introduction, this is also because such a Monte Carlo type approaches requires full inversions (to get ψ_{opt}^m) for each of the sample point $(u_i^*)^m$ and do not only involve direct simulations (i.e. evaluation of j) as in a forward propagation.

2.2. **Link with epistemic uncertainty.** Formulation (1)-(2) can also be used to quantify epistemic uncertainties considering u^* not as target data but as the state u^* corresponding to a first optimal solution ψ^*.

More precisely, let us proceed first with the solution of a minimization problem for f and find:

$$\psi^* = Argmin_{\psi \in \mathbf{O}_{ad}} f(\psi, u(\psi)).$$

Now, let us consider $u^* = u(\psi^*)$ and assume this is a random variable with known PDF. For simplicity, let us assume it is centered and Gaussian with variance σ a function of space. Larger values of σ are introduced where the model is known to be inadequate. In our situation, with the Saint Venant equations for instance, σ increases, for instance, toward the beaches. To account for the numerical discrepancies σ can also be, for instance, a function of the mesh and proportional to the linear interpolation error ($\sigma \sim L^t \mathbf{H}(u^*)L$) with L being a local vector characterizing the mesh (i.e. $L = (\delta x_{_1}, \delta x_{_2})$ locally defined involving local mesh size along directions $x_{_{i=1,2}}$ for a 2D structured mesh) and $\mathbf{H} = (\partial^2 u/\partial x_{ij})_{_{i,j=1,2}}$ the Hessian of the solution, here taken as a scalar function. The next step is to analyze the impact of this uncertainty on the solution of the minimization problem and eventually estimate the covariance matrix Cov_ψ knowing Cov_{u^*} through the second term in (2). We will discuss in the sequel two solutions to this question.

3. Low-complexity estimation of Cov_ψ

In the sequel, we discuss two low-complexity constructions of Cov_ψ the covariance matrix [57] of the bathymetry from Cov_{u^*} the covariance matrix of the data:

- section 4 shows how to use α-quantiles and directional extreme scenarios to build a first approximation to Cov_ψ,
- section 5 shows how to use a local linear relationship between the control parameter variations $\delta\psi$ and the state variations to provide an approximation to $Cov_{\delta\psi}$ and a second cumulative approximation to $diag(Cov_\psi)$.

We want these constructions to have a cost comparable to a deterministic inversion and we want to avoid any sampling of a large dimension space.

4. From α-quantiles and directional extreme scenarios to Cov_ψ

Our first construction uses the concept of α-quantile (denoted by VaR in the sequel) and directional extreme scenarios from which an estimation of the covariance matrix of the sea bottom ψ is obtained.

4.1. **Bounding the uncertainty domain using α-quantiles.** Consider a given random variable u with its PDF known (either analytic or tabulated). The tail of the PDF can be characterized defining for a given probability level ($0 < \alpha < 1$) the following threshold value:

$$\mathrm{VaR}_\alpha = \inf\{l \in \mathbb{R} : P(u > l) \leqslant 1 - \alpha\}.$$

Different α-quantile are available. One very well known is the Value at Risk (VaR) which has been widely used in financial engineering as a measure of risk of loss on a given asset [30]. Time dependency issue is interesting as it permits to account for possible improvement or degradation of measurement accuracy as discussed in [42, 45] or in the context of epistemic uncertainty quantification as described in section 2.1 for time dependent solutions.

With our quantile in hand, our aim is to define a closed domain of variation for the uncertain data. Given a threshold $0 \leqslant \alpha < 1$, the i^{th} component of the data $u^*_{i=1,\ldots,p} \in [\mu_i + \mathrm{VaR}^-_\alpha, \mu_i + \mathrm{VaR}^+_\alpha]$ with $\mathrm{VaR}^-_\alpha \leqslant 0 \leqslant \mathrm{VaR}^+_\alpha$ with probability α.

We have therefore, with probability α, an uncertainty domain for the data given by:

$$B_\alpha(\mu) = \Pi^p_{i=1}[\mu_i - 1.65\sigma_i, \mu_i + 1.65\sigma_i] \subset \mathbb{R}^p$$

In the case of Gaussian probability density functions we have $\mathrm{VaR}^-_\alpha = -\mathrm{VaR}^+_\alpha$ and the values at risk are explicitly known. For instance, with, respectively, $\alpha = 0.99$ and 0.95 we have $\mathrm{VaR}_{0.99}(\mathcal{N}(0,1)) = 2.33$, and $\mathrm{VaR}_{0.95}(\mathcal{N}(0,1)) = 1.65$, and $\mathrm{VaR}_\alpha(\mathcal{N}(0,\sigma)) = \sigma\mathrm{VaR}_\alpha(\mathcal{N}(0,1))$.

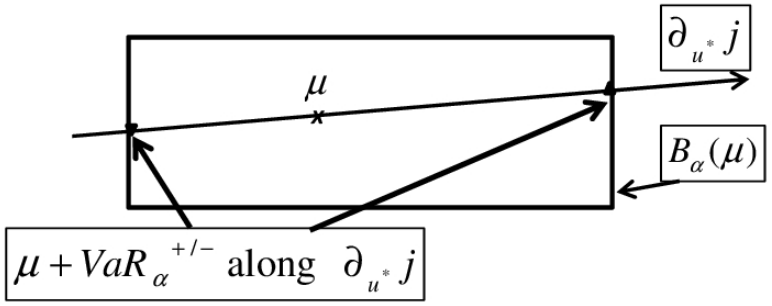

FIGURE 1. $(u^*)^{\pm}$ Directional extreme data sets as the intersection of $B_\alpha(\mu)$ and $d = \mu + t\ \partial_{u^*} j,\ t \in \mathbb{R}$.

4.2. **Directional Extreme Scenarios (DES).** $B_\alpha(\mu) \subset \mathbb{R}^p$ is a large dimensional domain and we cannot seriously consider any sampling of it. However, using the sensitivity of the functional with respect to the data we can identify two directional extreme sets of data corresponding to the intersection of $B_\alpha(\mu)$ and $d = \mu + \tau\ \partial_{u^*} j,\ \tau \in \mathbb{R}$ with $\mu = (\mu_1, ..., \mu_p)$. Let us call these two data sets $(u^*)^{\pm}$ defined by:

$$(u^*)_i^{\pm} = \mu_i \pm 1.65\ \sigma_i\ \left(\frac{\partial_{u^*} j}{\|\partial_{u^*} j\|}\right)_i, \quad i = 1, ..., p, \tag{3}$$

where we have assumed the data independent and their covariance matrix diagonal. $\partial_{u^*} j$ is easy to access for functional (2) as described in the next section. A sketch of this construction is shown in figure 1.

To measure the impact of this variability on the result of the minimization, we proceed with two deterministic gradient-based minimizations [29, 52] with an adjoint formulation for $\nabla_\psi j$ with the target data given by $(u^*)^{\pm}$. Let us call $(\psi^*)^{\pm}$ the results of these inversions: $(\psi^*)^{\pm} = Argmin_{\psi \in \mathbf{O}_{ad}} j(\psi, (u^*)^{\pm})$.

We have therefore three solutions $\psi^{\pm} = \{\psi^*, (\psi^*)^{\pm}\}$ for our optimization which can be used to provide confidence bounds for the deterministic inversion. This is a very small sampling of the domain of variation ψ would have due to the uncertainty on u^*. Still we think these are important points as we assume monotonic behavior for the outcome of the minimization with respect to the data which means that larger deviations in data bring larger variations in the outcome of the minimization. Also, this suggests that the maximum deviation for the results of the inversion due

to the uncertainty on the data can be estimated through $(\psi^*)^+ - (\psi^*)^-$. We consider the matrix $Cov_{\psi^\pm}$:

$$Cov_{\psi^\pm} = \mathbb{E}((\psi^\pm)(\psi^\pm)^t) - \mathbb{E}(\psi^\pm)\mathbb{E}(\psi^\pm)^t, \tag{4}$$

where the expectations are only evaluated over the sub-sampling $\psi^\pm$. We are in particular interested in the standard deviation for each of the components of ψ^* expressed through $diag(Cov_{\psi^\pm})^{1/2}$. We would like to compare these to $diag(Cov_\psi)^{1/2}$ build in the next section.

5. Adjoint-based covariance matrix of the bathymetry

We work in the context of a deterministic gradient based minimization using an adjoint formulation to access $\nabla_\psi j(\psi, u(\psi))$ with j given by (2) [47, 46]. We would like to take advantage of our adjoint calculation to estimate $diag(Cov_\psi)^{1/2}$.

5.1. Sensitivity evaluation.

Let us briefly recall the adjoint derivation for a generic state equation $F(u(\psi)) = 0$. The gradient of j with respect to ψ writes:

$$\nabla_\psi j = \frac{\partial j}{\partial \psi} + \left((\frac{\partial j}{\partial u})^t \ \nabla_\psi u \right)^t = \frac{\partial j}{\partial \psi} + \left((\frac{\partial j}{\partial u})^t \ (\nabla_u F)^{-1} \ \nabla_\psi F \right)^t = \frac{\partial j}{\partial \psi} + \left(v^t \ \nabla_\psi F \right)^t,$$

where we have introduced the adjoint variable v solution of:

$$(\nabla_u F)^t \ v = \frac{\partial j}{\partial u}. \tag{5}$$

In cases the governing equations are self adjoint (i.e. $\nabla_u F = (\nabla_u F)^t$), one can use the corresponding solver with $\frac{\partial j}{\partial u}$ as the right-hand side and simply solve:

$$\nabla_u F v = \frac{\partial j}{\partial u}.$$

Also, if F is linear, $\nabla_u F$ is a constant operator independent of u. The interest of the adjoint formulation is that the cost of getting $\nabla_\psi j$ becomes independent of the size of ψ. But, the problem with the adjoint approach is that, except for the two situations

we mentioned (linear or self adjoint state equations), it needs the development of a new code. This is why we use automatic differentiation when possible. We give an example of continuous adjoint derivation for a time dependent nonlinear problem in appendix.

In (2) the functional j involves the least-square deviation at data location between model and data. $\partial_u j$ in the right-hand side of (5) is a vector of size N and can be obtained writing:

$$j(\psi, u^*) = f(\psi, u(\psi)) + \frac{1}{2}\|\Pi u - u^*\|^2 = f(\psi, u(\psi)) + \frac{1}{2} < \Pi u - u^*, \Pi u - u^* >$$

$$= f(\psi, u(\psi)) + \frac{1}{2} < \Pi^t \Pi u, u > - < \Pi^t u^*, u > + \frac{1}{2} < u^*, u^* >,$$

and we have therefore

$$\partial_u j = \partial_u f + \Pi^t \Pi u - \Pi^t u^*.$$

On the other hand, $\partial_{u^*} j$ the sensitivity of j with respect to the data needed in (3) is a vector of size p. We consider $\partial_{u^*} j = \Pi^t \partial_u f(u^*) - (\Pi u - u^*) = \Pi^t \partial_u f(u^*)$ because we have taken $u^* = u(\psi^*)$ and the second term in (2) therefore vanishes as $\Pi u(\psi^*) = u^*$.

5.2. **From $\nabla_\psi j$ to Cov_ψ .** We would like to take advantage of our adjoint calculation leading to $\nabla_\psi j$ to estimate the covariance matrix of ψ.

Let us start establishing the expression for the covariance matrix of ψ considered as a vector of zero-mean random variables with independent components. This means we assume the covariance matrix diagonal which is fine as we are interested by its diagonal components.

Denote, for simplicity, by u the model solution (also zero mean valued: $u \leftarrow u - \mu$) at data location and suppose it is linked to the parameters through a linear model: $u = L\psi$. The covariance matrix for u is therefore:

$$Cov_u = \mathbb{E}(uu^t) = \mathbb{E}(L\ \psi\psi^t\ L^t) = L\ \mathbb{E}(\psi\psi^t)\ L^t = L\ Cov_\psi\ L^t.$$

If the dependency of u with respect to the parameter ψ is nonlinear the analysis still holds for the linearized model and the uncertainty on ψ can be reached accumulating those on successive $\delta\psi$ during our minimization procedure.

To illustrate the idea, let us consider the following sequence:

$$\psi_0 = given, \quad \psi_{k+1} = \psi_k + \delta\psi_k, \quad k = 0, ..., k_{max} - 1, \tag{6}$$

where $\delta\psi_k = -\rho\nabla_\psi j(\psi_k)$, for instance, in a descent method as we will see in sections 6 and 7. This sequence illustrates the path we take to go from the initial shape ψ_0 to the optimal one $\psi^* = \psi_{k_{max}}$.

Considering ψ_k and $\delta\psi_k$ as random variables we have (this is for each of their components):

$$\sigma^2(\psi_{k+1}) = \sigma^2(\psi_k + \delta\psi_k) = \sigma^2(\psi_k) + \sigma^2(\delta\psi_k) + 2Cov(\psi_k, \delta\psi_k). \tag{7}$$

This recurrence permits to accumulate the incremental variances.

Let us discuss how to evaluate $Cov_{\delta\psi}$ for a given couple $(\delta\psi, \delta u)$ omitting subscripts for simplicity. Introducing $\delta u = \mathcal{J}\delta\psi$ with $\mathcal{J} = \nabla_\psi u$ we have:

$$Cov_{\delta u} = \mathcal{J}\ Cov_{\delta\psi}\ \mathcal{J}^t.$$

To get $Cov_{\delta\psi}$ we need therefore to invert this expression and because the amount of data can be large and probably impossible to exactly fit, we proceed with a least-square formulation looking for $Cov_{\delta\psi}$ minimizing:

$$\frac{1}{2} < \mathcal{J}\ Cov_{\delta\psi}\ \mathcal{J}^t, \mathcal{J}\ Cov_{\delta\psi}\ \mathcal{J}^t > - < Cov_{\delta u}, \mathcal{J}\ Cov_{\delta\psi}\ \mathcal{J}^t > .$$

First order optimality condition with respect to $Cov_{\delta\psi}$ gives:

$$\mathcal{J}^t\mathcal{J}\ Cov_{\delta\psi}\ \mathcal{J}^t\mathcal{J} - \mathcal{J}^t\ Cov_{\delta u}\ \mathcal{J} = 0,$$

which leads to

$$Cov_{\delta\psi} = (\mathcal{J}^t\mathcal{J})^{-1}\ \mathcal{J}^t\ Cov_{\delta u}\ \mathcal{J}\ (\mathcal{J}^t\mathcal{J})^{-1},$$

and eventually, to

$$Cov_{\delta\psi} = \mathcal{J}^{-1}\, Cov_{\delta u}\, \mathcal{J}^{-t} = \left(\mathcal{J}^t\, Cov_{\delta u}^{-1}\, \mathcal{J}\right)^{-1}. \tag{8}$$

To get $Cov_{\delta\psi}$ and knowing $Cov_{\delta u}$, it is therefore sufficient to evaluate $\mathcal{J}$. The second expression in (8) is interesting as it involves the inversion of a $n \times n$ matrix and gives a least-square sense to the inversion of $N \times n$ matrices.

If the optimization is successful and model u and data u^* close, we can use the fact that data are usually independent and use the covariance matrix of the observation instead of Cov_u:

$$Cov_u \sim Cov_{u^*},$$

which is then diagonal and its inversion straightforward. The accumulation rule mentioned above can be applied to $Cov_{\delta u}$ as well giving:

$$\sigma^2(u^*) = \sigma^2(u_0 + \sum_{k=0}^{k_{max}-1} \delta u_k) = \sigma^2(u_0) + \sum_{k=0}^{k_{max}-1} \sigma^2(\delta u_k) + 2 \sum_{k=0}^{k_{max}-1} Cov(u_k, \delta u_k),$$

where $u_k = u_{k-1} + \delta u_{k-1}$ for $k > 0$. To simplify the calculation we assume zero uncertainty on the initial state (e.g. a uniform state), intermediate state variations independent from intermediate states (i.e. $Cov(u_k, \delta u_k) = 0$) and intermediate variances given by:

$$\sigma^2(\delta u_k) = \frac{1}{k_{max}} \sigma^2(u^*).$$

These assumptions guarantee that the total data variance $\sigma^2(u^*)$ is well preserved.

The question is therefore how to efficiently evaluate $\mathcal{J}$. The model at data locations Πu is obtained applying, for instance, a linear interpolation operator Π to the model solution u on the mesh. Therefore, we have:

$$\mathcal{J} = \Pi \nabla_\psi u.$$

Now recall that $\nabla_\psi j$ is available and has been computed with an adjoint approach in section 5.1. We now use it to access $\nabla_\psi u$ without extra calculation:

$$\nabla_\psi j = \frac{\partial j}{\partial \psi} + \left((\frac{\partial j}{\partial u})^t \ \nabla_\psi u \right)^t = \frac{\partial j}{\partial \psi} + \left((\frac{\partial j}{\partial u})^t \ \Pi^{-1} \mathcal{J} \right)^t ,$$

The first terms in the right-hand sides vanishes for (2) but is non-zero if, for instance, a Tykhonov regularization term is introduced in the functional [54]. This leads to:

$$(\frac{\partial j}{\partial u})^t \ \Pi^{-1} \mathcal{J} = (\nabla_\psi j - \frac{\partial j}{\partial \psi})^t,$$

and eventually to,

$$\mathcal{J} = \Pi \ (\frac{\partial j}{\partial u})^{-t} \ (\nabla_\psi j - \frac{\partial j}{\partial \psi})^t. \tag{9}$$

$(\partial j/\partial u)^{-t}$ is a vector of size N with components given by the inverse of those of $(\partial j/\partial u)$ divided by N in order to have $(\partial j/\partial u)^t.(\partial j/\partial u)^{-t} = 1$.

Alternatively, to avoid numerical difficulties with small components of $(\partial j/\partial u)$, (9) can again be seen in a least-square sense involving the inverse of the information matrix:

$$\mathcal{J} = \Pi \ \left((\frac{\partial j}{\partial u})(\frac{\partial j}{\partial u})^t \right)^{-1} \ \frac{\partial j}{\partial u} \ (\nabla_\psi j - \frac{\partial j}{\partial \psi})^t. \tag{10}$$

The information matrix is symmetric. If its condition number is large the Bunch and Kaufman [5] algorithm can be used writing the matrix as $PLDL^tP^t$ with P a permutation matrix, L unit-lower triangular and D block-diagonal with 1×1 or 2×2 blocks. The inversion hence only requires those of simple block-diagonal matrices. Also rank deficiency can be treated using the Moore-Penrose inverse based on the eigenvalue decomposition of the information matrix [8]. Under the hypothesis of the validity of the physical model, this analysis gives indications on the level of backward sensitivity of the optimization parameters with respect to the model solution which is also the sensitivity with respect of the deviation between the model and data at

the data locations as data are independent of ψ:

$$\nabla_\psi u = \nabla_\psi (u - u^*).$$

Because the cumulative rule (7) is for the variance, this construction only provides $diag(Cov_\psi)$ and not the full covariance matrix.

6. An illustrative model

Let us illustrate our purpose on a model problem for the interaction between the flow surface $h(t,x) : \mathbb{R}^+ \times [-100m, -20m] \to \mathbb{R}^+$ over a bed $\psi(t,x) : \mathbb{R}^+ \times [-100m, -20m] \to \mathbb{R}^+$ with $h \geqslant \psi$. The model expresses the changes in the bed with time due to elevations $h(t,x)$ and also how the flow elevation responds to the bed evolution.

We consider the following expression for h:

$$h(t,x) = h_0 + \beta \sin(\omega x (h_0 - \psi(t,x))),$$

where h_0 indicates the level at rest, β and ω are given such that $0 \leqslant \beta < 1$ and $\omega > 0$. This is a monochromatic wave, but superimposed waves can be considered as well without restriction. The bed is supposed initially flat $\psi(0,x) = \psi_0(x) = 1m$ and the water height at rest $h_0 = 1.3m$.

To close this model, we need to provide a model for $\psi(t,x)$. Introducing the bed velocity V, the bed motion can be seen through:

$$\partial_t \psi = -V(t,x)\partial_x \psi, \quad \psi(t=0,x) = \psi_0(x). \tag{11}$$

At this point we still need to link V to h. One can make the hypothesis that the bed adapts to the flow elevation in order to reduce the functional j:

$$\begin{aligned} j(\psi, h) &= \frac{1}{2h_0^2}(\|h(t,x)\|^2 + \|\psi - \psi_0\|^2) \\ &= \frac{1}{2h_0^2}\int_{-100}^{-20} (h^2(t,x) + (\psi - \psi_0)^2) dx. \end{aligned} \tag{12}$$

The scaling coefficient is chosen in order for $\nabla_\psi j$ to be dimensionless (here j and ψ are in meter).

The simplest path to minimize j is following:

$$
\begin{aligned}
&\partial_t \psi = -\rho \nabla_\psi j, \quad \psi(0,x) = \psi_0(x), \\
&\text{with} \quad \nabla_\psi j = j_\psi + j_h h_\psi \\
&\qquad\qquad = \left(-h\beta\omega x \cos(\omega x(h_0 - \psi)) + (\psi - \psi_0)\right)/h_0^2,
\end{aligned} \tag{13}
$$

where $\rho(m/s) \geqslant 0$ models the receptivity of the bed and is constant for a homogeneous bed. Larger ρ indicates larger bed porosity.

Considering the two expressions (11) and (13) for the evolution of ψ, the velocity V can now be expressed as $V(t,x) = \rho \nabla_\psi j / \partial_x \psi$. We have now a closed relation between h and ψ for given ρ which describes the bed characteristics. Figure 2 shows snapshots of h^*, ψ^* and V for an example of interactions starting from a flat bed and for an initial monochromatic wave. It shows how the coupling decreases the wave heights and therefore the wave energy. For regular beds, this model suggests that the bed velocity increases when the bed is or gets flat. In other words, flat beds appear being unstable which is something one observes in nature. Also, V has jumps where the bed is irregular. Finally V is bounded, for instance because of the orbital distribution of the motion of the fluid particles beneath the surface with decreasing velocity toward the bed. V cannot exceed this limit. The figure shows snapshots of an estimation of this bound V_{max} for the bed velocity V. One sees that the particles on the bed cannot move faster than at 5 cm/s. Establishing this bound is discussed in section 7 for a more sophisticated flow model.

Now that the model is defined and a first interaction between h and ψ analyzed giving the coupled solution (ψ^*, h^*), we would like to analyze the variability of the bed ψ^* due to uncertainty on the state h^* using the two approaches described in the previous sections. In both constructions, we assume having some knowledge of the state variability. Hence, we need to know σ_h and, as suggested in section 2.1, we can assume it proportional to the linear interpolation error together with a cut-off

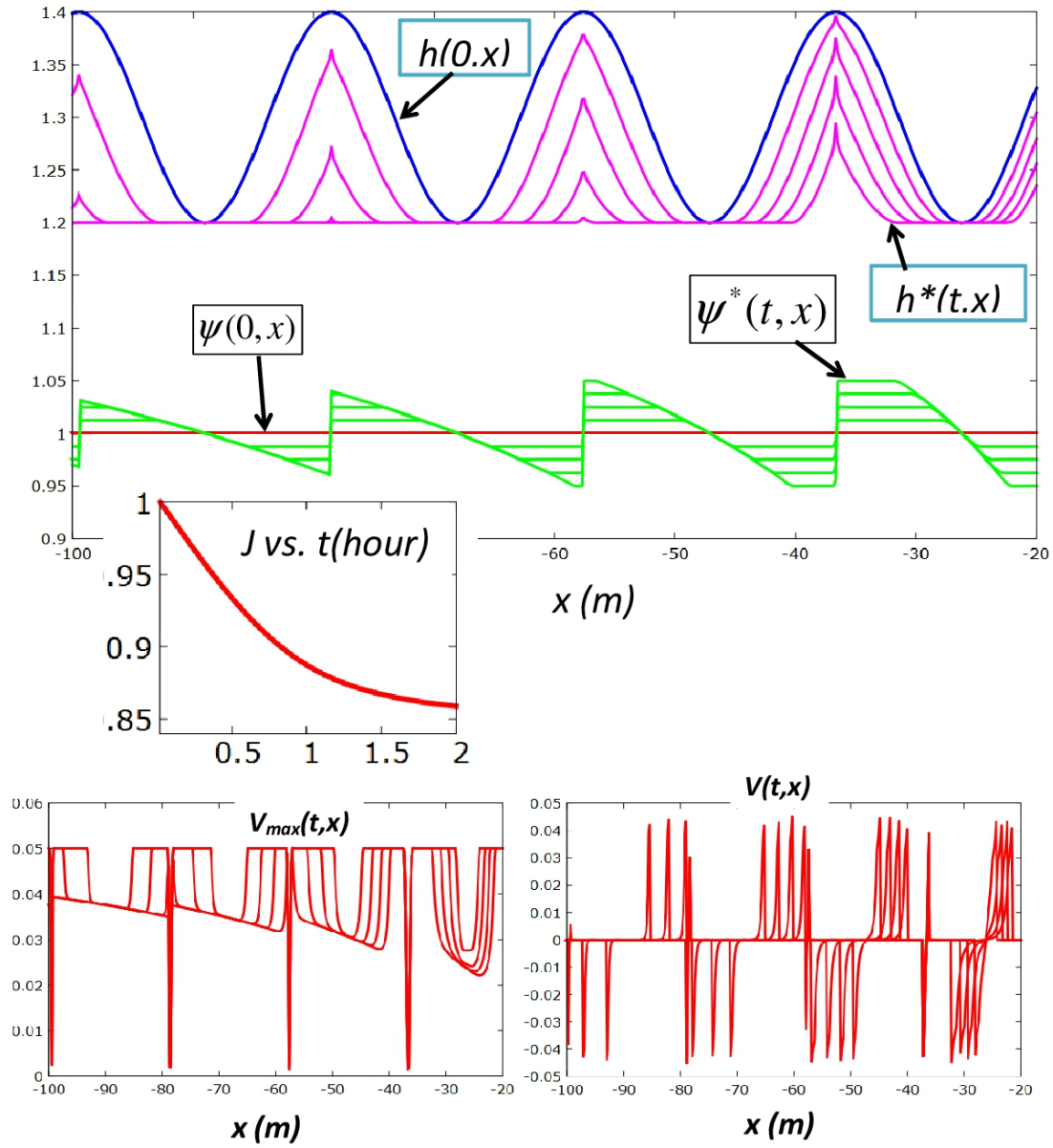

FIGURE 2. Snapshots of surface elevation $h^*(t,x)(m)$, bed $\psi^*(t,x)(m)$, maximum absolute bed velocity $V_{max}(t,x)(m/s)$ and bed velocity $V(t,x)(m/s)$ for the model of section 6. This corresponds to 2 hours of coupling minimizing functional (12). Initial (at $t = 0$) quantities are also shown.

to impose a minimum uncertainty level: $\sigma_h(t,x) = \delta x^2 \ \max(0.05, |\partial_x^2 h(t,x)|)$ with $\delta x \sim 0.8m$ being the mesh size for a 100 points mesh of the $[-100, -20]$ calculation domain. This is therefore a function of both time and space.

6.1. **Extreme scenarios.** The first construction builds extreme scenarios for h:

$$(h^*)^{\pm}(t,x) = h^*(t,x) \pm 1.65\ \sigma_h(t,x)\ \frac{\partial_{h^*} j}{\|\partial_{h^*} j\|}, \tag{14}$$

where $\partial_{h^*} j = h^*(t,x)/h_0^2$ and proceeds with two couplings minimizing respectively:

$$j^{\pm} = j + \frac{1}{2h_0^2}\|h(t,x) - (h^*)^{\pm}(t,x)\|^2, \tag{15}$$

giving two scenarios $(\psi^*)^{\pm}$. These scenarios permit to build an estimation of $\sigma_\psi(t,x) = diag(Cov_{\psi^{\pm}})^{1/2}$ using (4). This is shown in figure 3. One sees that a same level of uncertainty on the state h does not produce necessarily equidistributed variability on the bottom ψ. These constructions can take place at any time and not only at the end of the coupling. For instance, results in figure 3 are obtained after 30 minutes of coupling

6.2. Cov_ψ **matrix from** Cov_h**.** Let us pursue our construction of Cov_ψ following section 5 and compare its outcome to the previous extreme scenarios estimation of $diag(Cov_{\psi^{\pm}})^{1/2}$. Having in hand $\nabla_\psi j$ from (13) we follow the linear analysis and the cumulative construction presented in section 5 where the state u is replaced by h and where $k_{max} = 200$ iterations of coupling have been applied over more than two hours. The functional j is given by (12) and we have $\partial j/\partial\psi = (\psi - \psi_0)/h_0^2$ and $\partial j/\partial h = h/h_0^2$ and $\Pi = Id$ in (10) as the state is considered everywhere in the domain for the analysis. Figure 4 compares $diag(Cov_{\psi^{\pm}})^{1/2}$ and $diag(Cov_\psi)^{1/2}$. These constructions are compared to the result by an inverse Monte Carlo simulation described in section 2.1 with a sampling of size 1000. This is only feasible for such a simple model and it should be seen as a reference solution. The results show that the two approximations recover the right spatial distribution of the standard deviation with some over or underestimation of the maximum variability for ψ due, in one hand, to the cumulative nature of the variance in the second construction and, on the other hand, due to the reduced sampling used in the first. Overall one can consider that the constructions are useful for cheap backward uncertainty

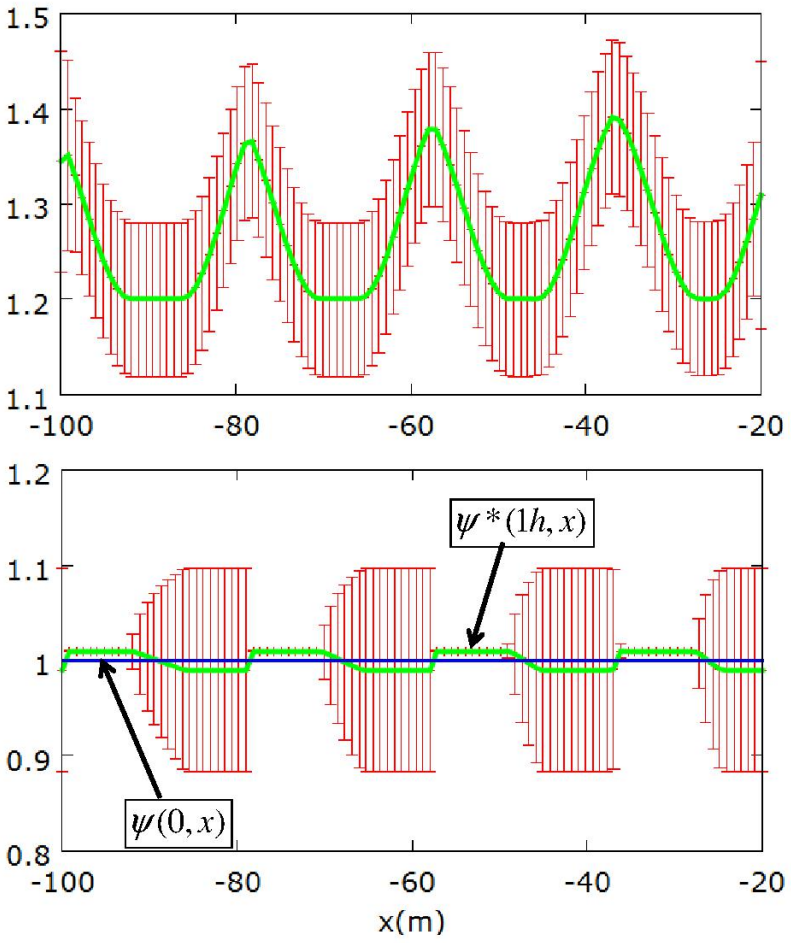

FIGURE 3. Upper: $h^*(t = 1h, x)$ and errorbars illustrating state variability through $\sigma_h(t = 1h, x)$. Lower: $\psi^*(t = 1h, x)$ and errorbars given by $\sigma_\psi = diag(Cov_{\psi^\pm})^{1/2}$.

quantification in situations where the Monte Carlo approach would be out of reach. We discuss this issue more extensively in the next section.

7. Uncertainty quantification for the evolution of the bed of a shallow water

Let us now discuss how the ingredients of the paper can be used to derive confidence bounds for the evolution of a shape under external forces. This is useful, for instance, in the definition of extreme scenarios in littoral erosion.

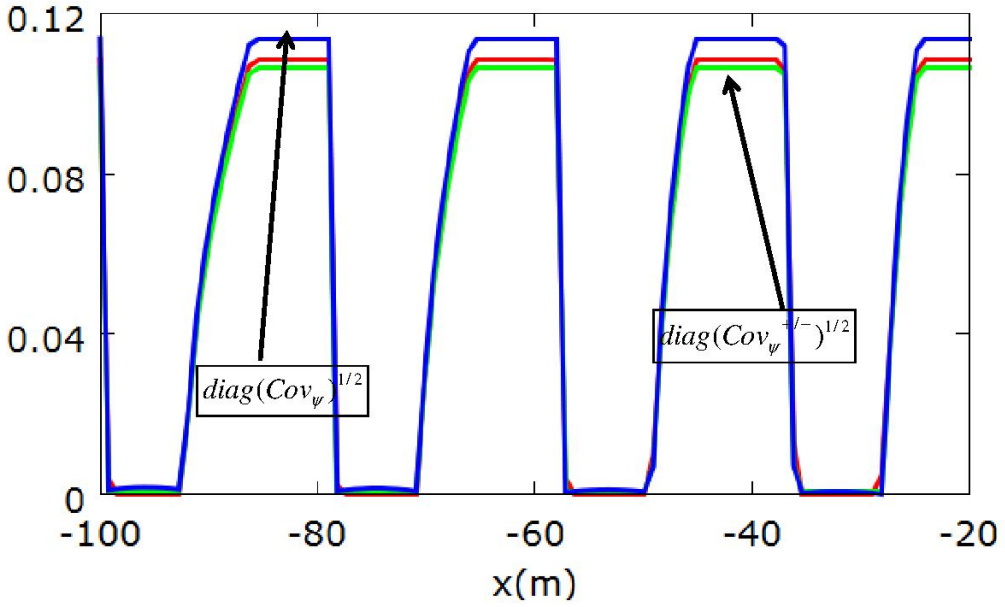

FIGURE 4. Comparisons between three constructions of $diag(Cov_\psi)^{1/2}$ (in meter) at the same instant. The DES estimation underpredicts and the cumulative adjoint based construction overpredicts the Monte Carlo prediction.

7.1. **Flow-bottom interactions.** We consider the interactions between the bottom of a shallow domain, seen as a soft shape, and the water motion described by shallow water equations. The sea bed ψ changes with time following the changes in the state given by the flow variables $\mathbf{U}$. We use a bed parameterization based on the bathymetry given at all the nodes of the fluid mesh [4, 3].

The model for the sea bed evolution is based on the minimization of a time dependent functional J involving the state evolution in time, solution of a state equation. We consider the Saint Venant shallow water equations as state equations for the fluid with $\mathbf{U} = {}^t(h, h\mathbf{u})$ where $\mathbf{u} = {}^t(u,\ v)$ is the depth-averaged velocity with u and v the scalar components in the horizontal directions and h the local water depth:

$$\partial_t \mathbf{U} + F(\mathbf{U}, \psi) = 0, \text{ with initial and boundary conditions,}$$

where

$$F(\mathbf{U},\psi) = \begin{pmatrix} \nabla.(h\mathbf{u}) \\ \nabla.(h\mathbf{u}\otimes\mathbf{u}) + gh\nabla(h+\psi) \end{pmatrix}, \tag{16}$$

where $g(m.s^{-2})$ is acceleration due to the gravity.

As in our illustrative problem of section 6, J is minimized looking for the evolution in time of ψ following:

$$\partial_t\psi = -\rho(t,x)\nabla_\psi J,\ \ \psi(t=0,x) = \psi_0(x) = \text{given}, \tag{17}$$

where $\rho(t,x)$ is a positive parameter which depends on the local porosity of the bed and quantify its receptivity to flow perturbations. The physical time scales for the fluid and structure (bed motion) are quite different. Indeed, flows have time scales of the order of seconds and the sea bed motion takes place over hours.

The cost function involves the state evolution as, for instance, in:

$$J = K\int_{t-T}^{t} j(\psi,\mathbf{U}(\psi,\tau))d\tau, \tag{18}$$

where T indicates a time dependency window and also permits to introduce a difference in time scales between sea bed and flow motions. The scaling K is to make $\nabla_\psi J$ dimensionless. One looks for the bed acting as a flexible structure and adapting to the flow conditions in order to minimize some energy-based functional. In [3, 4] we consider a functional made of the L^2 norm of the deviation of the wave elevation from a low frequency component by a moving average over a time interval T:

$$\eta(t,x) = h(t,x) - \overline{h}(t,x) \quad \text{with} \quad \overline{h}(t,x) = \frac{1}{T}\int_{t-T}^{t} h(\tau,x)d\tau, \tag{19}$$

and involving a constraint on sand displacements requiring minimal bottom changes from the bathymetry $\psi(t-T)$ at the beginning of a time interval of influence $[t-T,t]$:

$$J = \frac{1}{|\Omega|^{1/2}Th_0^2}\int_{t-T}^{t}\int_{\Omega}\left(\eta^2 + (\psi(\tau,x) - \psi(t-T,x))^2\right)\ d\tau d\Omega, \tag{20}$$

where Ω is the observation domain and h_0 is the water level at rest.

If the simulation takes place in a closed domain Ω the amount of the material making the bed must be conserved:

$$\int_\Omega \partial_t \psi \; d\omega = 0 \text{ or } \int_\Omega \psi \; d\omega = \text{constant}, \tag{21}$$

which is a global constraint on the shape. In [45] we showed why this constraint implies that a basin experience cannot represent the evolution of a bottom in open sea and that the conclusions of such experiences should not simply be extended to open sea sites.

Also, as in the model problem, an equivalent bed velocity can be defined:

$$\partial_t \psi = -V(t,x)\nabla_x \psi \quad \text{with} \quad V = (\rho \nabla_\psi J/\partial_{x_1}\psi, \rho \nabla_\psi J/\partial_{x_2}\psi). \tag{22}$$

This permits to provide upper bounds for local bed deformation velocity using the orbital velocity damping function [53]:

$$\varphi(x, x_3) = \frac{\cosh(k(x)(h(x) + x_3(x)))}{cosh(k(x)h(x))},$$

where x_3 indicates the vertical direction with $x_3 = -h(x)$ being the bottom at location $x = (x_1, x_2)$ and $k(x) = 2\pi/\lambda(x)$ the wave number. Figure 5 shows three instances of φ over the depth for different wave numbers.

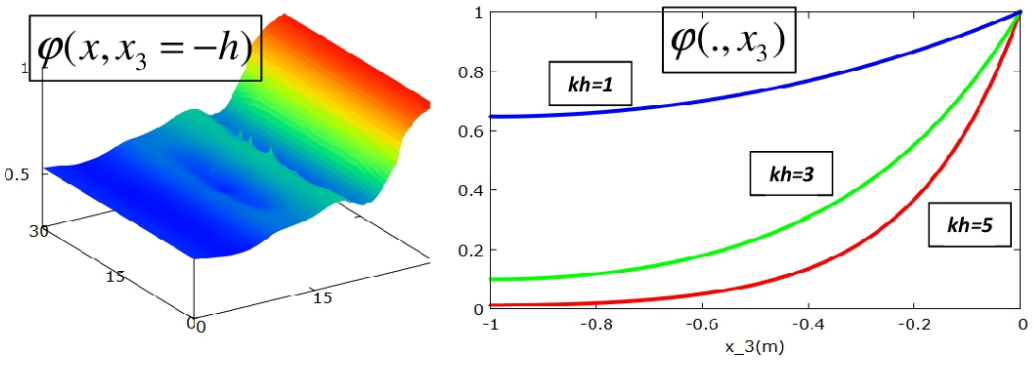

FIGURE 5. $\varphi(., x_3)$ (right) describes how the orbital velocity diminishes with water depth for different wave numbers and its application to the bottom shown in figure 6.

However, in the context of a Saint Venant model getting $\lambda(x)$, and therefore $k(x)$, is not simple as the simulation only provides instantaneous vertically mean valued quantities. We introduce a linear approximation for the decay of $\lambda(x)$ toward the beach:

$$\lambda(x) \sim \lambda(x_{in}) \max(0.1, \frac{\|x - \Gamma_b\|}{\|x_{in} - \Gamma_b\|}),$$

where $\|x-\Gamma_b\|$ is the distance of a given point to the beach Γ_b (i.e. where $h \leqslant 10^{-3}$) and $\|x_{in}-\Gamma_b\|$ the distance of a given point on the inlet boundary Γ_{in} to the beach. In frozen bed simulations for the cases discussed here, a posteriori analysis gives a value of $h(x_{in}) \sim 4m$ and $k(x)h(x)$ between 1 and 4. Using these information, we make the following assumption for the maximal gradient-based local shape deformation:

$$|\partial_t \psi| \leqslant \max(\varphi(x, x_3 = -h) \left(|u\partial_{x_1}\psi| + |v\partial_{x_2}\psi|\right), 0.1\|\mathbf{u}(x)\|).$$

The lower cutoff becomes active when the bed is or becomes flat which we saw is an unstable situation [45]. Figure 5 shows the damping orbital function $\varphi(x, x_3 = -h)$ for the simulation shown in figure 6. As this estimation is destined to establish bounds for the instantaneous bed deformation dynamics, an accurate definition is not necessary. Actually, this should be seen as a source of uncertainty to be accounted for in the definition of the uncertainty on the bed deformation. This uncertainty can be combined together with the uncertainty on the bed receptivity $\rho(t, x)$, for instance, using quantile-based scenarios as shown in [45, 42]. In this work we assume ρ constant which means the bed is constituted of a single sand type.

7.2. **Shallow water solver.** Shallow water equations are discretized by a finite volume formulation [51]. Our finite volume implementation preserves steady state solutions on non flat sea beds in the absence of perturbations [15, 2]. It is also suitable for the capture of wetting and drying phenomena [17, 36]. Four boundary conditions are needed at slip, inlet, shoreline and outlet boundaries. The slip boundary condition ($\mathbf{u}.\mathbf{n} = 0$) is naturally taken into account in a finite volume formulation. The outlet condition is a transmissive boundary condition. Values at boundary cells

are obtained by second order extrapolations normal to the boundary from the values inside the domain. To describe incoming waves we use an absorbing/generating inlet boundary condition where the values of water depth are prescribed. In subcritical regimes, characteristic curves and Riemann invariants provide normal velocity. In open sea we allow for reflected waves to freely exit the domain [48]. This is another major difference between basin experiments and open sea. A numerical simulation of a basin can account for outgoing waves but an experimental set up cannot. In our implementation the waves are produced on the inlet boundary where the water wave elevation is represented by the addition of N monochromatic waves:

$$h(t) = h_0 + 2A \sum_{i=1,..,N-1} \sin\left(\frac{\omega_i + \omega_{i+1}}{2} t\right) \cos\left(\frac{\omega_i - \omega_{i+1}}{2} t\right), \tag{23}$$

with h_0 being the water height at rest, A the inlet water wave amplitude and $\omega_i = 2\pi/T_i$ the wave pulses[2].

7.3. **Flow in a basin.** Let us consider Ω to be the Sogreah 3D wave basin in Grenoble (France) which is a square of side 30 m already mentioned in [4, 3, 45]. Figure 6 shows the initial bottom depth linearly increasing cross-shore. The incoming waves (23) are defined with $h_0 = 0.75m$, $A = 0.12m$. We consider two modes with periods T_1 of $3.5s$ and T_2 of $2.5s$. The time scale of coupling between the fluid motion and changes in the bed is taken as $T = 3.5s$. This means that several time steps are taken in the flow solver (several hundreds because of the CFL condition in the shallow water solver $\delta t \leqslant 0.5\delta x/(\|\mathbf{u}\| + \sqrt{gh})$) before a new time step by the bed model corresponding to one minimization iteration. Figure 6 shows the solution (ψ^*, h^*) after more than two hours of coupling. This corresponds to $k_{max} \sim 800$ iterations of coupling as we take $T = 3T_1$ in 20. This is an a priori choice and also a source of uncertainty. It is present in any coupling strategy. Unlike with a numerical spatial mesh size or time step, one cannot make it go to zero as there will be no interaction then. On site observations suggest the coupling should take place at every few water waves. The bottom variations decrease when the system achieves an equilibrium

[2]More realistic conditions can be applied following a Jonswap distribution [10].

between the flow perturbations and the bottom motion. One sees in particular that the model predicts long shore sand bars damping the wave energy; something which corresponds to on site observations.

Figure 7 shows three instances of the normalized equivalent bottom velocity V given by (22) illustrating the instantaneous directions of the motion of the bed. One sees that the adjoint based bottom deformation is equivalent to a transport model for the bathymetry with an advection velocity bearing very complex patterns both long and cross-shore. These are instantaneous snapshots and show non intuitive equivalent instantaneous bottom velocity fields while the final bottom shown in figure 6 features longshore sand bars observed in nature and low longshore variability. This is despite we did not enforce the conservation constraint (21). This is an indication of why basin experiments cannot correctly represent open sea phenomena. Indeed, to represent open sea we would need transparent boundary conditions there instead of symmetry representing slipping walls. However, the equivalent bottom velocity snapshots clearly show both cross and longshore sand transports along lateral boundaries incompatible with a lateral slip boundary condition.

7.4. Cov_ψ **and** $Cov_{\psi^\pm}$**.** Now we would like to proceed with the quantification of the uncertainties on $\psi^*(t,x)$ following what has been presented for our model problem.

The first construction builds extreme scenarios for the water height. This also induces variability on the velocity through the shallow water equations. As in our model problem, knowing $\sigma_h(t,x)$ we consider two scenarios around $h^*(t,x)$:

$$(h^*)^\pm(t,x) = h^*(t,x) \pm 1.65\ \sigma_h(t,x)\ \frac{\partial_{h^*} J}{\|\partial_{h^*} J\|}, \tag{24}$$

with J given by (20) and proceed with two couplings minimizing respectively:

$$J^\pm = J + \frac{1}{|\Omega|^{1/2} T h_0^2} \int_{t-T}^{t} \int_\Omega (\Pi h(t,x) - \Pi(h^*)^\pm(t,x))^2\ d\tau d\Omega, \tag{25}$$

giving two scenarios $(\psi^*)^\pm$. But, if $\Pi = Id$, this would require the storage of all instances of $h^*(t,x)$ which is very challenging. At this point, we need therefore a

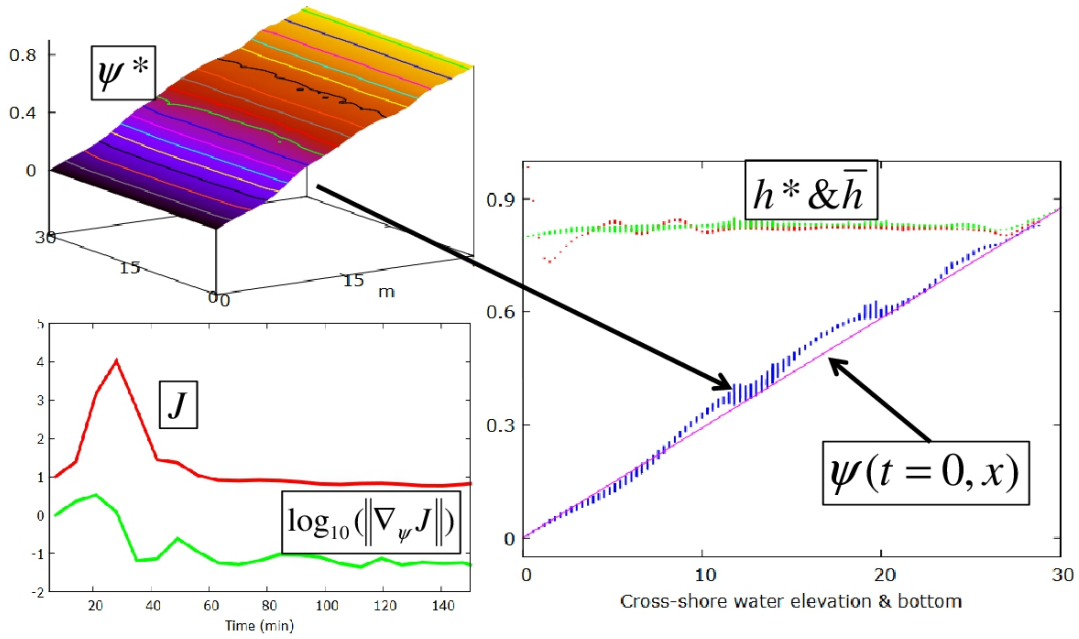

FIGURE 6. Initial bottom $\psi(0,x)$, coupled solution (h^*,ψ^*) after more than two hours of interaction and the moving averaged water level $\eta = \overline{h}$. Vertical bars indicate longshore variability. Normalized histories of J and $\nabla_\psi J$ show that the system reaches some equilibrium.

low-storage solution to make the approach viable. One alternative is to only consider q snapshots and Π will then be an indicator function $\Pi = \mathbf{1}_{\{t_i, i=1,\dots,q\}}$. But, this will bring new questions on the robustness and sensitivity of the approach with respect to the choice of these snapshots. The solution we adopt is to consider for Π the moving average operator which is linear and therefore makes that the analysis presented in sections (5.1) and (5) remains valid. This is also physically sound as the average water level is an important quantity in erosion and submersion phenomena and deterministic prediction must account for the uncertainty on this quantity. Hence, we consider:

$$J^{\pm} = J + \frac{1}{|\Omega|^{1/2} T h_0^2} \int_{t-T}^{t} \int_{\Omega} (\overline{h}(t,x) - (\overline{h^*})^{\pm}(t,x))^2 \, d\tau d\Omega, \tag{26}$$

where $(\overline{h^*})^{\pm}$ is built applying (19) to (24):

$$(\overline{h^*})^{\pm}(t,x) = \overline{h^*}(t,x) \pm 1.65\frac{1}{T}\int_{t-T}^{t} \sigma_h(\tau,x)\ \frac{\partial_h J(h^*)}{\|\partial_h J(h^*)\|}d\tau$$

Which reduces to:

$$(27)\quad (\overline{h^*})^{\pm}(t,x) = \overline{h^*}(t,x) \pm 1.65\frac{1}{T}\int_{t-T}^{t} \sigma_h(\tau,x)\ \tilde{\eta}(\tau,x)\ d\tau \quad \text{with} \quad \tilde{\eta} = \eta^*/\|\eta^*\|.$$

To close this model, we need to provide an expression for $\sigma_h(t,x)$ which can account for both aleatoric or non reducible and epistemic or reducible variability on the state. We assume zero mean Gaussian uncertainty for h^* with $\sigma_h(t,x)$ linearly increasing toward the beach. This is justified, in one hand, by the fact that the shallow water equations are not valid when h tends to zero and, on the other hand, because we assume the uncertainty on the characteristics of the incoming waves (the inlet boundary condition) is propagated and amplified by the model toward the beach. In all cases, as shown in figure 6 the largest variability cross-shore on $\overline{h^*}$ is reached in the swash zone. Of course, this is illustrative and other assumptions can be made for σ_h assimilating, for instance, available on site observations. We assume $\sigma_h(t,x)$ is given by:

$$(28)\qquad \sigma_h(t,x) = \sigma_{in}\ \frac{\overline{h}^{1+\delta}(t,\Gamma_{in})}{\overline{h}^{1+\delta}(t,x)+\varepsilon}\ (\gamma\frac{\|x-x_{in}\|}{\|\Gamma_b - x_{in}\|}+1),$$

with typical values of $\sigma_{in} = 0.03m$, $\gamma = 2$, $0 < \delta(= 0.2)$, $\varepsilon = 10^{-3}$ and with $\overline{h}(t,\Gamma_{in})$ being the mean water height along the inlet boundary. The dependency in $\overline{h}$ is to avoid $\lim_{\tilde{h}\to 0} \sigma_h(t,x)\ \tilde{h} = 0$ toward the beach which would mean no uncertainty there.

Figure 8 shows the covariance matrix $Cov_h = diag\,(\sigma_h^2)$ with σ_h given by (28). σ_{in} needs to be compared to $h_0 = 0.75m$ in our simulation which means we assume about 4% variability in the mean water height. This perturbation already produces non negligible effects on the bottom. This means that a rise of 3-5% of the sea level can produce noticeable environmental impacts as it is accompanied by an important increase in the energy of the system. Figure 9 shows the two extreme scenarios

$(h,\psi)^{\pm}$ minimizing $J^{\pm}$ given by (26) after one hour. Curves are for the mean water height and the bathymetry with indication of longshore variability. These scenarios give a first estimation of the impact of the uncertainty on the water height on the bathymetry.

These scenarios permit to build an estimation of the covariance matrix for ψ using (4). Figure 10 shows $diag(Cov_{\psi^{\pm}})^{1/2}$ after $60min$. One sees that a same level of uncertainty on the state h shown in figure 9 does not lead to similar variability distribution for the bottom ψ. This can be seen, for instance, along a parallel line to the shore along which the uncertainty on the state is constant.

Finally, the extreme scenarios covariance construction $Cov_{\psi^{\pm}}$ is compared to the cumulative adjoint-based construction Cov_{ψ} given in section 5 and previously applied to a model problem in section 6.2. As in the model problem, both constructions recover similar spatial distribution of the standard deviation. We cannot afford here an inverse Monte Carlo simulation for comparison. As we expect the cumulative approach to over-estimate the variance levels, the two constructions can be seen providing lower and upper bounds for the standard deviation. Also both constructions identify important sensitivity along the lateral boundaries which is another reason basin experiments should not be used to represent open seas.

Finally, despite the state variability $\sigma_h(t,x)$ is assumed maximum in the swash zone, the bottom variability appears quite low there. Let us consider the following relative variability with respect to the mean water depth. This quantity permits to better highlight the variability in the swash zone. It shows that the highest impact is near and along the swash area and actually in some places up to 40% of the bathymetry predicted by the deterministic simulation. The adjoint based construction also predicts high relative variability just before the swash zone. The figure also compares the longshore distributions of the two estimations of the relative variabilities. In all cases, this suggests the importance of providing with any deterministic prediction serving in the definition of beach protection guidelines an

indication of the associated uncertainties, especially if the interest is on beach lines morphodynamics.

8. Application with other bed models

The ingredients of the paper have been illustrated with a variational model for the bed motion used in both the model problem and also together with the shallow water equations:

$$\psi_t = -\rho \nabla_\psi J, \quad \psi(t=0,x) = \psi_0. \tag{29}$$

This approach has been previously introduced in [3, 4]. It is based on the application of control theory to the evolution of a low stiffness structure coupled with a fluid using minimization principles. The fundamental assumption is that the bed adapts to the flow by some sort of minimal sand transport in order to minimize some energy expression.

But the discussion of the paper on the impact of flow state uncertainties is not limited to such a model. Indeed, one well-known approach to model sea bed motion is through the Exner equation [50]. Also, many techniques have been proposed to solve the system of Saint-Venant and Exner equations [2, 26, 55]. Below, we show that our variational model has a similar interpretation.

The Exner equation models the conservation of mass between the bed and transported sediments.

$$\psi_t = -\frac{1}{1-\lambda_p} \nabla . q, \quad \psi(t=0,x) = \text{given}, \tag{30}$$

where $\lambda_p \in [0,1[$ is the porosity of the bed and q is the flux of transported sediments. To estimate this flux q, scientists propose a variety of formula such as the Meyer-Peter & Müller or Gras formulas [22]. The former suggests that the flux q is directly related to the shear stress and the latter to the fluid velocity .

ρ in our minimization equation (29) should increase with the porosity of the bed. Indeed, one expects the influence of a same flow condition on a bed to grow for lighter sands and to be none for rocky beds (i.e. nearly no porosity). Hence, we consider the following relationship between ρ and λ_p:

$$\rho(1-\lambda_p) = \rho_r = cste,$$

where we typically consider $\rho_r = 0.001 m/s$. Let us suppose that the porosity is constant everywhere (i.e. bed of a same sand), then we simply have:

$$\nabla.q = \rho_r \nabla_\psi J, \tag{31}$$

where $\nabla.$ is the divergence in space and ∇_ψ the gradient with respect to the shape ψ. Consider a one dimensional situation. Our minimization approach is equivalent to an Exner equation with a nonlocal expression for q:

$$q(t,x) = q(t,-\infty) + \rho_r \int_{-\infty}^{x} \nabla_\psi J(t,\zeta) d\zeta,$$

where without harm one can suppose $q(t,-\infty) = 0$ and $\nabla_\psi J(t,\zeta) \to 0$ when $\zeta \to -\infty$ as the influence of the flow on the bed decreases offshore with the flow depth increasing. The nonlocal term depends on the choice of the cost function. Similar nonlocal terms can be found, for instance, in two models for the motion of sand dunes sheared by a fluid flow [18, 34]. In these models, the nonlocality only concerns the space and there is no minimal transport issue involved. The time scale T in (18) permits to better focus on the differences in the time scales between sea bed and flow motions. It is derived in order for the computed mean water level to coincide with on site observations.

9. Concluding remarks

An original procedure for the quantification of the impact of state uncertainties in littoral erosion has been presented and it has been shown how confidence margins

can be established for the sea bed evolution predicted by deterministic high-fidelity simulations.

Two low-complexity backward uncertainty quantification constructions have been proposed. These are generic and can be used with any deterministic beach morphodynamic platform. Both have been thought in order for the cost of the analysis to remain comparable to the original deterministic prediction. This makes them attractive and permits to consider high-fidelity simulation tools and avoids reduced order modeling usually used in UQ.

Also the approaches have been requested to only use what already available in terms of code and not to require intense new developments. This makes them comparable to Monte Carlo type constructions in term of coding complexity. The first approach uses PDF quantiles and builds directional extreme scenarios from which an approximation of the shape covariance matrix is obtained. This approximation is compared to an incremental construction using a local linear relationship between the optimization parameter and the state and the adjoint of the functional.

The constructions have been illustrated on a model problem for this fluid-structure interaction and a more sophisticated model involving the Saint Venant shallow water equations. The conclusion is that both approaches seem to give good estimation of the spatial distribution of the standard deviation for the bathymetry. However, due to its cumulative nature, the second approach seems to overestimate the variance levels compared to inverse Monte Carlo predictions. This suggests that the uncertainties do not sum up necessarily here. This approach rather corresponds to a worst-case estimation of the variance and provides upper bounds for the variance. On the other hand, because it is based on a reduced sample, the extreme scenarios construction rather provides lower bounds. With these bounds in hand two situations can be considered. Either the two estimations are close, which a posteriori confirms that the considered reduced sample well represents the extreme scenarios. This is of major interest from an engineering point of view and the bounds can be used for the quantification of the impact of state uncertainties on the bed evolution.

Or the estimations are very different, in which case the worst-case estimation, even rough, is still of interest for risk management while the reduced sampling should be considered with great caution as some important scenarios are probably missing.

Also, it has been discussed why conclusions from basin experiments cannot simply be extended to open seas situations. This is annoying as most of industrial designs in coastal engineering for sand beaches is still experimental based. We are not in the situation of wind tunnels or anechoic chambers where the effort mainly goes to the minimization of the influences of the boundaries. Here we have an extra difficulty with the sand conservation constraint induced by basin experiments which does not exist in open sea situations.

From a broader point of view this work enters the domain of epistemic and aleatoric uncertainty quantification for shape optimization for unsteady fluids. It permits to quantify our confidence on an optimal shape without any sampling of a large dimensional parameter space.

Acknowledgments: The adjoint Saint Venant solver has been obtained using `Tapenade` AD tool developed at INRIA-Sophia Antipolis by L. Hascoet and his team Tropics. The autour would like to express his gratitude to Dr. F. Bouchette of Montpellier GeoSciences Laboratory for his feedback on this work physical aspects.

10. Appendix: Sensitivity evaluation by adjoint

Sensitivity evaluation in large dimension needs an adjoint variable approach to make the cost of the evaluation independent from the size of the control space. In time dependent problems, this implies storage of all intermediate states which can be optimized by check-pointing technics [23, 24]. This appendix briefly describes the adjoint method with a time dependent state equation (the Saint Venant equations in our case).

Let us consider the following formal dependency chain:

$$\psi \to \{\mathbf{U}(\psi, \tau), \tau \in [0, T]\} \to J(\psi, T).$$

Here, ψ is the independent variable and $\mathbf{U}$ and J are the dependent ones. $\mathbf{U}(\psi,\tau)$ are solutions in time of

$$\partial_t \mathbf{U} + F(\mathbf{U},\psi) = 0,\ \mathbf{U}(0) = \mathbf{U}_0(\psi). \tag{32}$$

To be accurate, one should also consider the independent physical parameters such as those describing the waves. But, this would have introduced unnecessary complications into the notations.

Consider a functional involving an integral over time:

$$J(\psi,T) = \int_{(0,T)} j(\psi,\mathbf{U}(\psi,t)).$$

Linearizing J gives:

$$J_{_\psi}(\psi,T) = \int_{(0,T)} (j_{_\psi} + j_{\mathbf{U}}\mathbf{U}_{_\psi}).$$

In this expression only $\mathbf{U}_{_\psi}$ is costly to get as it requires the linearization of the shallow water equations.

The linearized state equation:

$$\partial_t(\mathbf{U}_{_\psi}) + F_{_\psi}(\mathbf{U},\psi) + F_{\mathbf{U}}(\mathbf{U},\psi)\mathbf{U}_{_\psi} = 0,\ \mathbf{U}_{_\psi}(0) = \mathbf{U}'_0(\psi), \tag{33}$$

permits to write for all function $\mathbf{V}$ (where $\mathbf{V}$ has the same structure than $\mathbf{U}$):

$$0 = \int_{(0,T)\times\Omega} (\partial_t(\mathbf{U}_{_\psi}) + F_{_\psi}(\mathbf{U},\psi) + F_{\mathbf{U}}(\mathbf{U},\psi)\mathbf{U}_{_\psi})\ \mathbf{V}.$$

Introducing the adjoint operator $F^*_{\mathbf{U}}$, it gives:

$$0 = \int_{(0,T)\times\Omega} (-\partial_t\mathbf{V} + F^*_{\mathbf{U}}(\mathbf{U},\psi)\ \mathbf{V})\mathbf{U}_{_\psi} + \int_\Omega [\mathbf{V}\mathbf{U}_{_\psi}]_0^T + \int_{(0,T)\times\Omega} \mathbf{V}F_{_\psi}(\mathbf{U},\psi).$$

Let us introduce a backward adjoint problem:

$$\partial_t\mathbf{V} + F^*_{\mathbf{U}}(\mathbf{U},\psi)\mathbf{V} = j_{\mathbf{U}}, \qquad \mathbf{V}(T) = 0. \tag{34}$$

Therefore, with $\mathbf{V}$ solution of the backward adjoint equation (34) with the chosen final condition one has:

$$\int_{(0,T)\times\Omega} j_{\mathbf{U}}\mathbf{U}_{\psi} = \int_{\Omega} \mathbf{V}(0)\mathbf{U}_0'(\psi) - \int_{(0,T)\times\Omega} \mathbf{V}F_{\psi}(\mathbf{U},\psi).$$

If there is no direct dependency between the initial condition $\mathbf{U}(0)$ and ψ the first term in the right-hand-side vanishes. Also, for the Saint Venant equations the direct dependency in ψ is in $gh\nabla\psi$ in the equations for $h\mathbf{u}$, see (16). Denoting $\mathbf{V} = (v_1, \mathbf{v_2})^t$ with $\mathbf{v_2}$ the adjoint variable associated to $\mathbf{u}$, one has in weak form:

$$\int_{(0,T)\times\Omega} \mathbf{V}F_{\psi}(\mathbf{U},\psi) = -\int_{(0,T)\times\Omega} g\nabla.(h\mathbf{v_2}).$$

As described in section 7.2 we use either slip or Dirichlet boundary conditions for the velocity which give for the corresponding adjoint variable slip or homogeneous Dirichlet conditions removing the boundary term in the weak form. We see that, unlike with the linearized equation, with ψ of any dimension $\mathbf{V}$ is computed only once. One remarks however that states $\mathbf{U}$ are needed in reverse order because the backward integration in (34). The previous analysis has been implemented by automatic differentiation [24, 46, 47] applied to our shallow water solver. `Tapenade` uses advanced checkpointing techniques to address the previous storage issue [9, 25, 44].

References

[1] AIAA. Guide for the verification and validation of computational fluid dynamics simulations. *AIAA*, G-077, 1998.

[2] E. Audusse and MO. Bristeau. A well-balanced positivity preserving second order scheme for shallow water flows on unstructured meshes. *JCP*, 206:311–333, 2005.

[3] A. Bouharguane and B. Mohammadi. Optimal dynamics of soft shapes in shallow waters. *Computers and Fluids*, 40/1:291–298, 2011.

[4] A. Bouharguane and B. Mohammadi. Minimization principles for the evolution of a soft sea bed interacting with a shallow sea. *IJCFD*, 26/3:163–172, 2012.

[5] J. R. Bunch and L. Kaufman. Some stable methods for calculating inertia and solving symmetric linear systems. *Mathematics of Computation*, 31(137):163–179, 1997.

[6] J. Caers. *Modeling Uncertainty in the Earth Sciences*. Wiley-Blackwell, 2011.

[7] G. Casella and R. Berger. *Statistical Inference, 2nd Ed.* Duxbury Press, London, 2001.

[8] P. Courrieu. Fast computation of moore-penrose inverse matrices. *CoRR*, abs/0804.4809, 2008.

[9] B. Dauvergne and L. Hascoët. The data-flow equations of checkpointing in reverse automatic differentiation. In *Lecture Notes in Computer Science Vol. 3994, Proceedings ICCS 2006*, pages 566–573, Reading, UK, 2006. Springer.

[10] M. Dunckel D.E. Hasselmann and J.A. Ewing. Directional wave spectra observed during jonswap 1973. *Journal of Physical Oceanography*, 10/8:1264–1280, 1980.

[11] R.G. Dean and R. A. Dalrymple. *Water Wave Mechanics for Engineers and Scientists*. World Scientific Publishing, 1991.

[12] R.G. Dean and R. A. Dalrymple. *Coastal processes with Engineering Applications*. Cambridge University Press, 2004.

[13] J. Dronkers. *Dynamics of Coastal Systems*, volume 25 of *Adv. Ser. Ocean Eng.* World Scientific Publishing, Singapore, 2005.

[14] A. Bouharguane et al. Low complexity shape optimization and a posteriori high fidelity validation. *Disc. Cont. Dyn. Syst. B.*, 13:759–772, 2010.

[15] E. Audusse et al. A fast and stable well-balanced scheme with hydrostatic reconstruction for shallow water flows. *SIAM J.Sci.Comp.*, 25/6:2050–2065, 2004.

[16] G. Evensen. *Sequential Data Assimilation for Nonlinear Dynamics: The Ensemble Kalman Filter In Ocean Forecasting: Conceptual basis and applications*. Springer-Verlag, Heidelberg, 2002.

[17] P. Fabrie F. Marche, Ph. Bonneton and N. Seguin. Evaluation of well-ballanced bore-capturing schemes for 2d wetting and drying processes. *IJNMF*, 53/5:867–894, 2007.

[18] A.C. Fowler. Dunes and drumlins. In N.J. Balmforth and A. Provenzale, editors, *Geomorphological fluid mechanics*, pages 430–454. Springer, Berlin, 2001.

[19] R. Ghanem and A. Doostan. On the construction and analysis of stochastic models: characterization and propagation of the errors associated with limited data,. *J. of Comput. Phys.*, 217:63–81, 2006.

[20] R. Ghanem and P. Spanos. *Stochastic Finite Elements: A Spectral Approach*. Springer Verlag, New York, 1991.

[21] M. Giles. Multilevel monte carlo methods. *Acta Numerica*, 24:259–328, 2015.

[22] A.J. Gras. Sediment transport by waves and currents. SERC London Cent. Mar. Techno, Report No: FL29 (1981).

[23] A. Griewank. *Computational derivatives*. Springer, New York, 2001.

[24] L. Hascoet and V. Pascual. Tapenade user's guide. In *INRIA Technical report*, pages 1–31. INRIA, 2004.

[25] L. Hascoët and V. Pascual. The Tapenade automatic differentiation tool: Principles, model, and specification. *ACM Transactions on Mathematical Software*, 39(3):20:1–20:43, 2013.

[26] J. Hudson and P. Sweby. Formulations for numerically approximating hyperbolic systems governing sediment transport. *J. Sci. Comput.*, 19:225–252, 2003.

[27] P. Azerad F. Bouchette D. Isebe and B. Mohammadi. Optimal shape design of coastal structures minimizing short waves impact. *Coastal Engineering*, 55/1, 2008.

[28] P. Azerad F. Bouchette D. Isebe and B. Mohammadi. Shape optimization of geotextile tubes for sandy beach protection. *IJNME*, 74:1262–1277, 2008.

[29] B. Ivorra and B. Mohammadi. Optimization strategies in credit portfolio management. *Journal of Global Optimization*, 43/2:415–427, 2009.

[30] Ph. Jorion. *Value at Risk: The New Benchmark for Managing Financial Risk*. McGraw-Hill, New York, 2006.

[31] M. Ghil K. Ide, P. Courtier and A. Lorenc. Unified notation for data assimilation: operational, sequential and variational. *Journal of the Meteorological Society of Japan*, 75/1B:181–189, 1997.

[32] R.E. Kalman. A new approach to linear filtering and prediction problems. *Transactions of the ASME - Journal of Basic Engineering*, 82:35–45, 160.

[33] K.C. Kapur and L.R. Lamberson. *Reliability in Engineering Design*. John Wiley & Sons, New York, 1997.

[34] K.K.J. Kouakou and P-Y. Lagree. Evolution of a model dune in a shear flow. *Eur. J. Mech. B Fluids*, 25/3:348–359, 2006.

[35] F. Lindsten and T. B. Schn. Backward simulation methods for monte carlo statistical inference. *Machine Learning*, 6:111–143, 2013.

[36] F. Marche and Ph. Bonneton. A simple and efficient well-balanced scheme for 2d bore propagation and run-up over a sloping beach. In *Proceedings of Int. Conf. Coast. Eng. ICCE*, pages 143–152. Springer, 2006.

[37] C.C. Mei. *The applied dynamics of ocean surface waves*. World Scientific Publishing, 1989.

[38] S. Mishra, Ch. Schwab, and J. Sukys. Multilevel Monte Carlo finite volume methods for shallow water equations with uncertain topography in multi-dimensions. 34(6):B761–B784, ???? 2012.

[39] B. Mohammadi. Reduced sampling and incomplete sensitivity for low-complexity robust parametric optimization. *Int. J. Num. Meth. Fluids*, 73/4:307–323, 2013.

[40] B. Mohammadi. Principal angles between subspaces and reduced order modeling accuracy in optimization. *Structural and Multidisciplinary Optimization*, 50/2:237–252, 2014.

[41] B. Mohammadi. Uncertainty quantification by geometric characterization of sensitivity spaces. *Compt. Meth. Appl. Mech. Eng.*, 280:197–221, 2014.

[42] B. Mohammadi. Value at risk for confidence level quantifications in robust engineering optimization. *Optimal Control: Applications and Methods*, 35/2:179–190, 2014.

[43] B. Mohammadi. Ensemble kalman filters (enkf) and geometric characterization of sensitivity spaces for uncertainty quantification in optimization. *Computer Methods in Applied Mech. & Eng.*, 290:228–249, 2015.

[44] B. Mohammadi. Parallel reverse time integration and reduced order models for efficient adjoint lattice boltzmann methods. *SMAI J. of Computational Mathematics*, 1:5–28, 2015.

[45] B. Mohammadi and F. Bouchette. Extreme scenarios for the evolution of a soft bed interacting with a fluid using the value at risk of the bed characteristics. *Computer & Fluids*, 89:78–87, 2014.

[46] B. Mohammadi and O.Pironneau. *Applied Shape Optimization for Fluids (2nd Edition)*. Oxford Univ. Press, Oxford, 2009.

[47] B. Mohammadi and O. Pironneau. Shape optimization in fluid mechanics. *Annual Revue of Fluid Mechanics*, 36/1:255–279, 2004.

[48] GS. Desilva N. Kobayashi and KD. Watson. Wave transformation and swash oscillation on gentle and steep slopes. *J. Geophys. Res.*, 94:951–966, 1989.

[49] P. Nielsen. *Coastal and Estuarine Processes*. World Scientific Publishing, Singapore, 2002.

[50] C. Paola and V. R. Voller. A generalized exner equation for sediment mass balance. *J. Geophys. Res.*, 110:1–8, 2005.

[51] T. Gallouët R. Eymard and R. Herbin. *Finite volume methods*, volume VII of *Handbook of numerical analysis*. North Holland, Amsterdam, 2000.

[52] P. Redont and B. Mohammadi. Improving the identification of general pareto fronts by global optimization. *CRAS*, 347:1–8, 2009.

[53] R.L. Soulsby. Calculating bottom orbital velocity beneath waves. *Coastal Engineering*, 11/4:371–380, 1987.

[54] A. Tarantola. *Inverse problem theory and methods for model parameter estimation*. SIAM, N.Y., 1987.

[55] A. Valiani V. Caleffi and A. Bernini. High-order balanced cweno scheme for movable bed shallow water equations. *Advances in Water Resources*, 30:730–741, 2007.

[56] X. Wan and G.E. Karniadakis. Multi-element generalized polynomial chaos for arbitrary probability measures. *SIAM J. Sci. Comput.*, 28/3:901–928, 2006.

[57] L. Wasserman. *All of Statistics: A Concise Course in Statistical Inference*. ISBN 0-387-40272-1. Springer, 2004.

[58] D. Xiu. *Numerical Methods for Stochastic Computations: A Spectral Method Approach*. Princeton University Press, 2010.

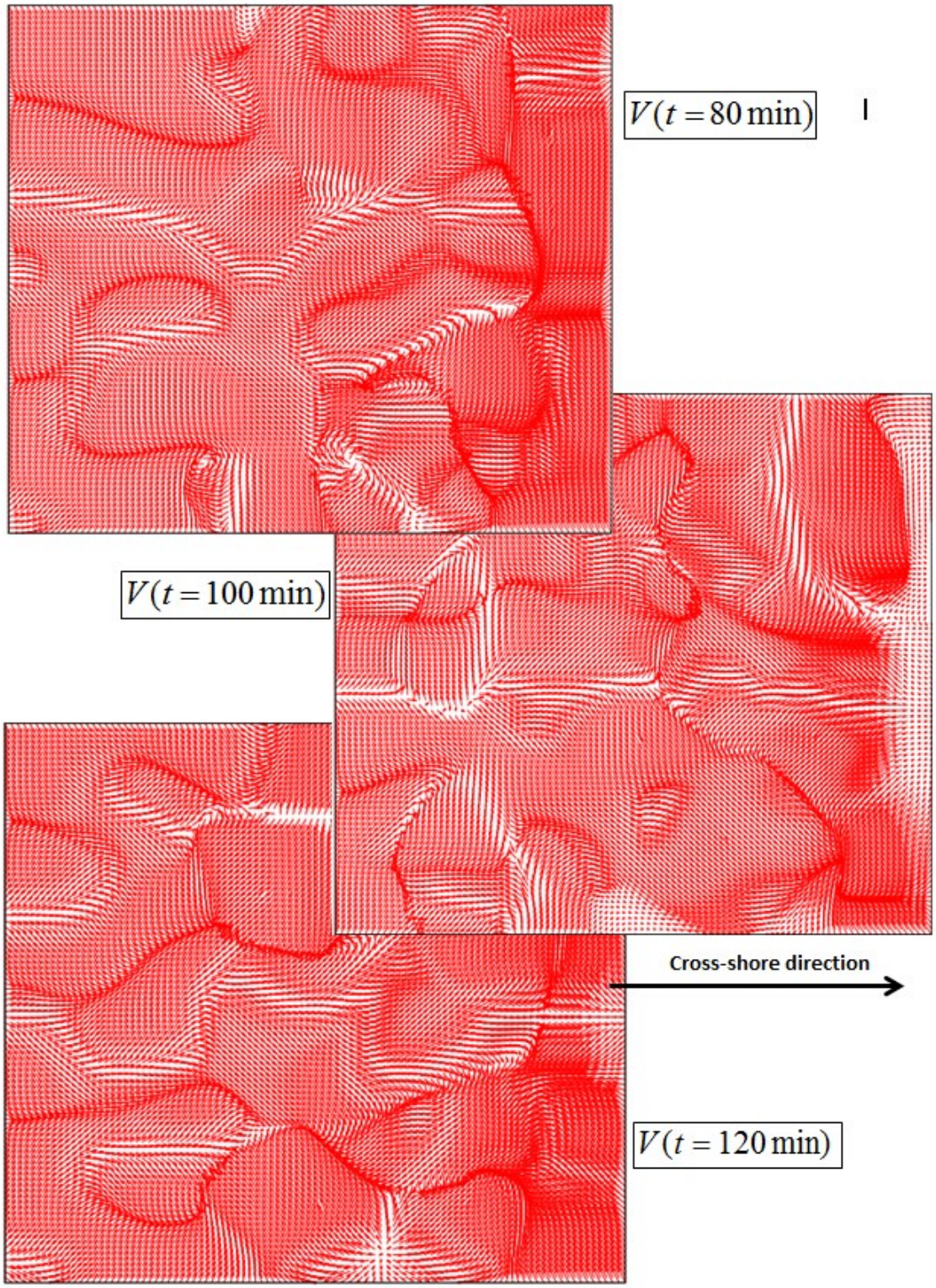

FIGURE 7. Three instances of $V/\|V\|$ with V the equivalent bottom velocity given by (22). This indicates the instantaneous directions of the motion of the bed. Complex directions pattern appear with both long and cross-shore variability.

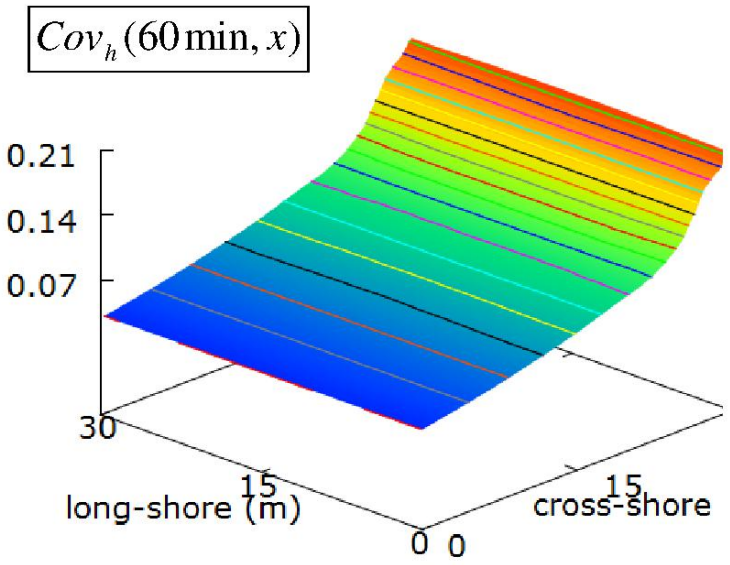

FIGURE 8. Covariance matrix $Cov_h = diag\,(\sigma_h^2)$ with σ_h given by (28).

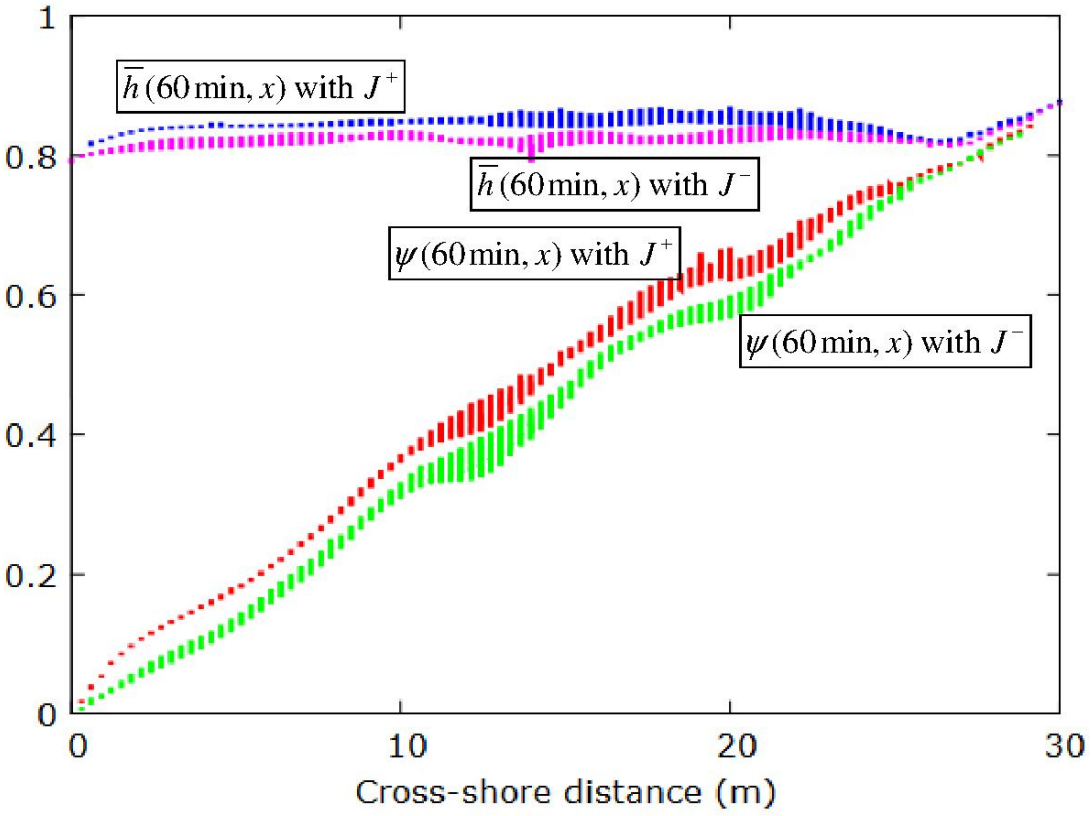

FIGURE 9. $(h, \psi)^{\pm}$ are two extreme scenarios obtained minimizing $J^{\pm}$ given by (26). The picture shows the moving average over T of the water height h and the bottom ψ for each of the scenario after one hour accounting for the uncertainty on the water height introduced through the covariance matrix Cov_h shown in picture 8.

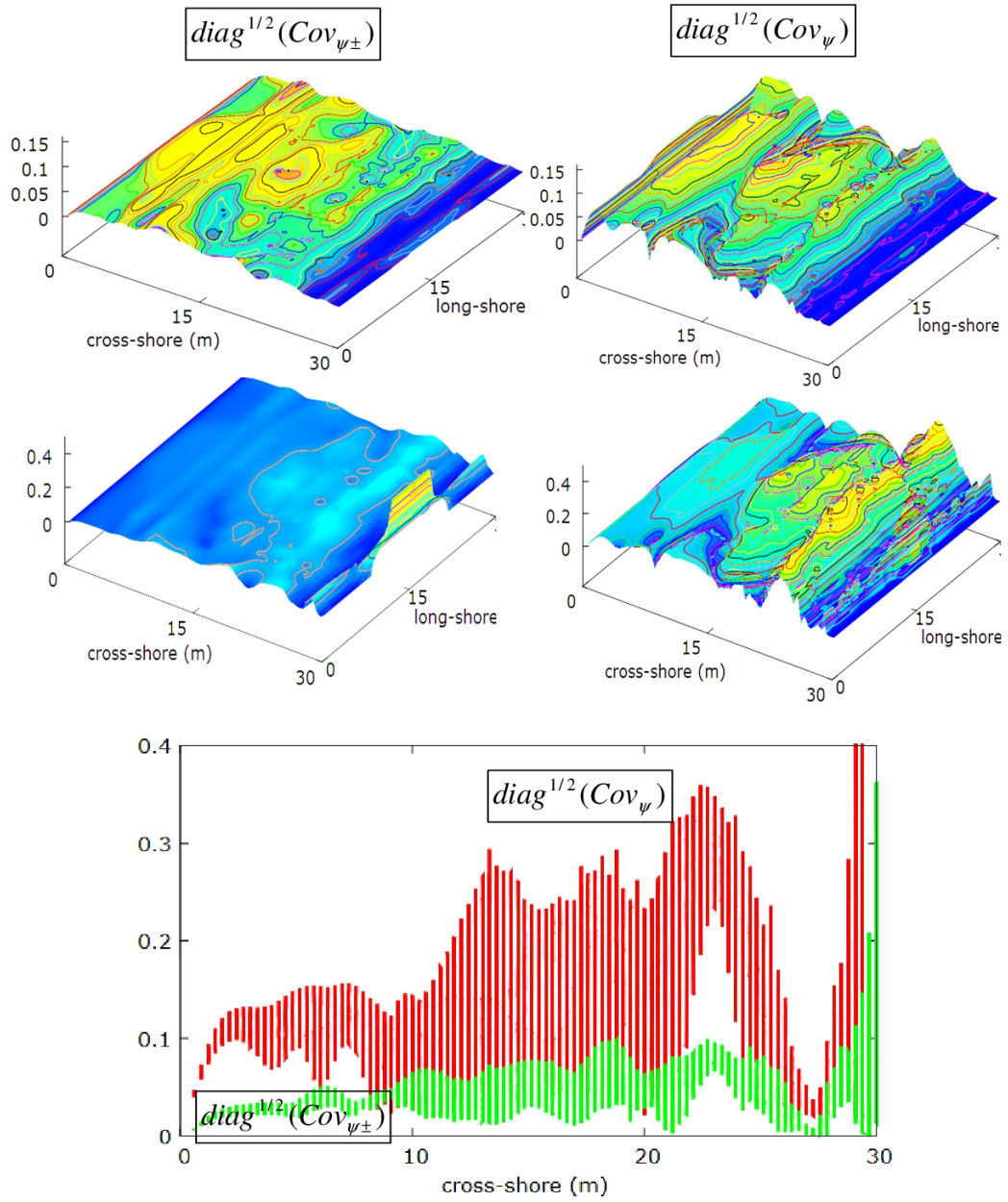

FIGURE 10. $diag(Cov_{\psi\pm})^{1/2}$ (left column) and $diag(Cov_{\psi})^{1/2}$ (right column) after $60min$ of coupling. Upper pictures show absolute variabilities and middle pictures relative ones with respect to the mean water depth. Relative variability shows that the highest impact is near and along the swash zone and up to 40% of the bathymetry predicted by the deterministic simulation. Lower picture compares the two bounds and illustrates their longshore distribution.